Chapter

Compact Incoherent Multidimensional Imaging Systems Using Static Diffractive Coded Apertures

Vijayakumar Anand, Soon Hock Ng, Tomas Katkus, Daniel Smith, Vinoth Balasubramani, Denver P. Linklater, Pierre J. Magistretti, Christian Depeursinge, Elena P. Ivanova and Saulius Juodkazis

Abstract

Incoherent holographic imaging technologies, in general, involve multiple optical components for beam splitting—combining and shaping—and in most cases, require an active optical device such as a spatial light modulator (SLM) for generating multiple phase-shifted holograms in time. The above requirements made the realization of holography-based products expensive, heavy, large, and slow. To successfully transfer the holography capabilities discussed in research articles to products, it is necessary to find methods to simplify holography architectures. In this book chapter, two important incoherent holography techniques, namely interference-based Fresnel incoherent correlation holography (FINCH) and interferenceless coded aperture correlation holography (I-COACH), have been successfully simplified in space and time using advanced manufacturing methods and nonlinear reconstruction, respectively. Both techniques have been realized in compact optical architectures using a single static diffractive optical element manufactured using lithography technologies. Randomly multiplexed diffractive lenses were manufactured using electron beam lithography for FINCH. A quasi-random lens and a mask containing a quasi-random array of pinholes were manufactured using electron beam lithography and photolithography, respectively, for I-COACH. In both cases, the compactification has been achieved without sacrificing the performances. The design, fabrication, and experiments of FINCH and I-COACH with static diffractive optical elements are presented in details.

Keywords: Fresnel incoherent correlation holography, coded aperture imaging, diffractive optics, electron beam lithography, photolithography, imaging, high-speed imaging, quasi-random lens, scattering, self-interference, incoherent imaging

1. Introduction

The invention of holography has revolutionized the field of imaging in numerous ways [1–3]. The capability to record complete three-dimensional (3D) amplitude and phase information of an object from a few camera recordings is a remarkable advantage for many applications. In coherent holography, the light diffracted from an object is interfered with a reference wave derived from the same source to form the hologram of the object. With a coherent source such as a laser, the above task can be achieved in any of the standard interferometry architectures [4]. In the recent years, there has been a shift in focus from using coherent light sources to incoherent ones due to many advantages such as low cost, high SNR and high resolution. In incoherent holography, due to lack of coherence, the hologram cannot be formed by interfering object wave with reference wave but between two differently modulated object waves [1]. The above interference is called self-interference. Achieving such a configuration was a challenging task in the past and many sophisticated architectures such as rotating shear interferometer [5], triangle interferometer [6], and conoscopic holography [7] were developed. With the advent of active devices, such as spatial light modulators, realization of incoherent holography systems became relatively easier. Some notable incoherent holography techniques with active devices include Fresnel incoherent correlation holography (FINCH) [8], Fourier incoherent single-channel holography (FISCH) [9], and self-interference digital holography (SIDH) [10]. Of all the above three methods, FINCH and FISCH can exhibit super resolution while SIDH in off-axis configuration cannot. FINCH requires the simplest and compact optical configuration of the above three methods with a high field of view. Due to the above reasons, FINCH became an attractive imaging system [11–15] and moved successfully to industry as powerful 3D fluorescence microscopy products: FINCH^{TM} and CINCH^{TM} [16].

Another research direction called coded aperture imaging (CAI) using incoherent illumination evolved alongside of FINCH [17, 18]. In CAI, the light from an object is modulated by a coded aperture and the intensity distribution is recorded. The recorded intensity distribution is reconstructed into object's image either by using the transmission function of the coded aperture or by using the recorded point spread function. The first reports of CAI came in 1968 using random array of pinholes to perform lensless imaging of X-rays and Gamma rays [19, 20]. However, the image reconstruction was noisy due to the computational reconstruction mechanism. So, CAI evolved in search of the coded aperture–computational reconstruction (CA-CR) compatible pair that can create object's images with a high quality. During this search, uniformly redundant array (URA)-based coded aperture was found to exhibit a high signal-to-noise ratio in comparison to random array of pinholes [21]. Later, modified URA (MURA) with two shots was found to perform better in signal-to-noise ratio [22]. In this direction, by designing an appropriate CA-CR pair, spatio-spectral imaging methods, such as coded aperture snapshot spectral imager (CASSI), were developed [23, 24]. The CASSI approach was later expanded by applying compressive sensing methods [25]. In 2011, optical imaging using a phase coded aperture was reported [26]. There are multiple patents awarded on CAI methods for developing compact imaging products and in some cases, CAI has been used as an assistive technology in a larger framework.

The FINCH technique has a relatively low axial resolution in comparison to lens-based imaging and so coded aperture correlation holography (COACH) was developed in 2016 from FINCH by modifying the beam modulations [27]. In FINCH, the

light from an object was modulated by two quadratic phase masks with different focal distances and the resulting two different object waves were interfered to form the hologram. In COACH, the light from a point is modulated by a quasi-random phase mask and a constant phase mask and interfered to form the hologram. In FINCH, at least three camera shots were recorded with different phase-shifts between the two interfering beams and combined into a complex hologram in order to cancel the twin image and bias terms. This complex hologram was numerically propagated to one of the focal planes of the quadratic phase mask to reconstruct the object information. In COACH, the phase mask is random and therefore, there is no focal plane where the hologram can be propagated. So, in COACH, the complex hologram was reconstructed by cross-correlating it with the complex point spread hologram recorded for different depths. In COACH, the lateral and axial resolutions are therefore given by the lateral and axial correlation lengths governed by the numerical aperture as in the case of lens-based imaging. During the development of COACH, it was identified that two-beam interference was not needed to record 3D information of the object, which led to the development of non-interferometric or interferenceless COACH (I-COACH) [28]. The development of I-COACH linked the capabilities of incoherent holography with the simplicity of CAI. The connection became evident after the demonstration of a super-resolution I-COACH method using specially coded apertures that generate random array of sub-diffraction and a lateral resolution approaching that of FINCH [29].

As a matter of fact, the current state-of-the-art FINCH as well as I-COACH technology are not optimal. The FINCH™ and CINCH™ still require numerous optical components and active devices, which makes the implementation challenging and as a product, less attractive and expensive. In I-COACH, or in general CAI, the requirements are less but the challenges lie in the lower efficiency of coded aperture and limited applications. During the past years, at Nanolab of Swinburne University of Technology (SUT), we have been working on expanding FINCH and I-COACH beyond the current state-of-the-art technologies using static diffractive optical elements manufactured using advanced fabrication technologies [30–34]. In this book chapter, we present the design, fabrication, and implementation of static diffractive optical elements in FINCH and I-COACH. Furthermore, we also present a conceptual configuration using static diffractive optical elements for optical trapping and imaging.

2. Fresnel incoherent correlation holography (FINCH)

2.1 Methodology and simulation results

FINCH was developed by Rosen and Brooker in the year 2007 [8]. The optical configuration of FINCH is shown in **Figure 1a**. Light from an object point is split into two waves using an SLM in which a phase mask formed by a random multiplexing of two quadratic phase functions with different focal lengths was displayed. These two object waves were interfered to form the object hologram. As FINCH is in in-line configuration, at least three object holograms need to be recorded with relative phase shifts of $\Theta = 0, 2\pi/3$, and $4\pi/3$ radians and combined in complex space to remove the twin image and bias terms during reconstruction by numerical backpropagation. Let us consider a point object with an amplitude of $\sqrt{I_o}$. The complex amplitude at a distance of z_1 from the point and entering the SLM is given as $C_1\sqrt{I_o}Q(1/z_1)$, where

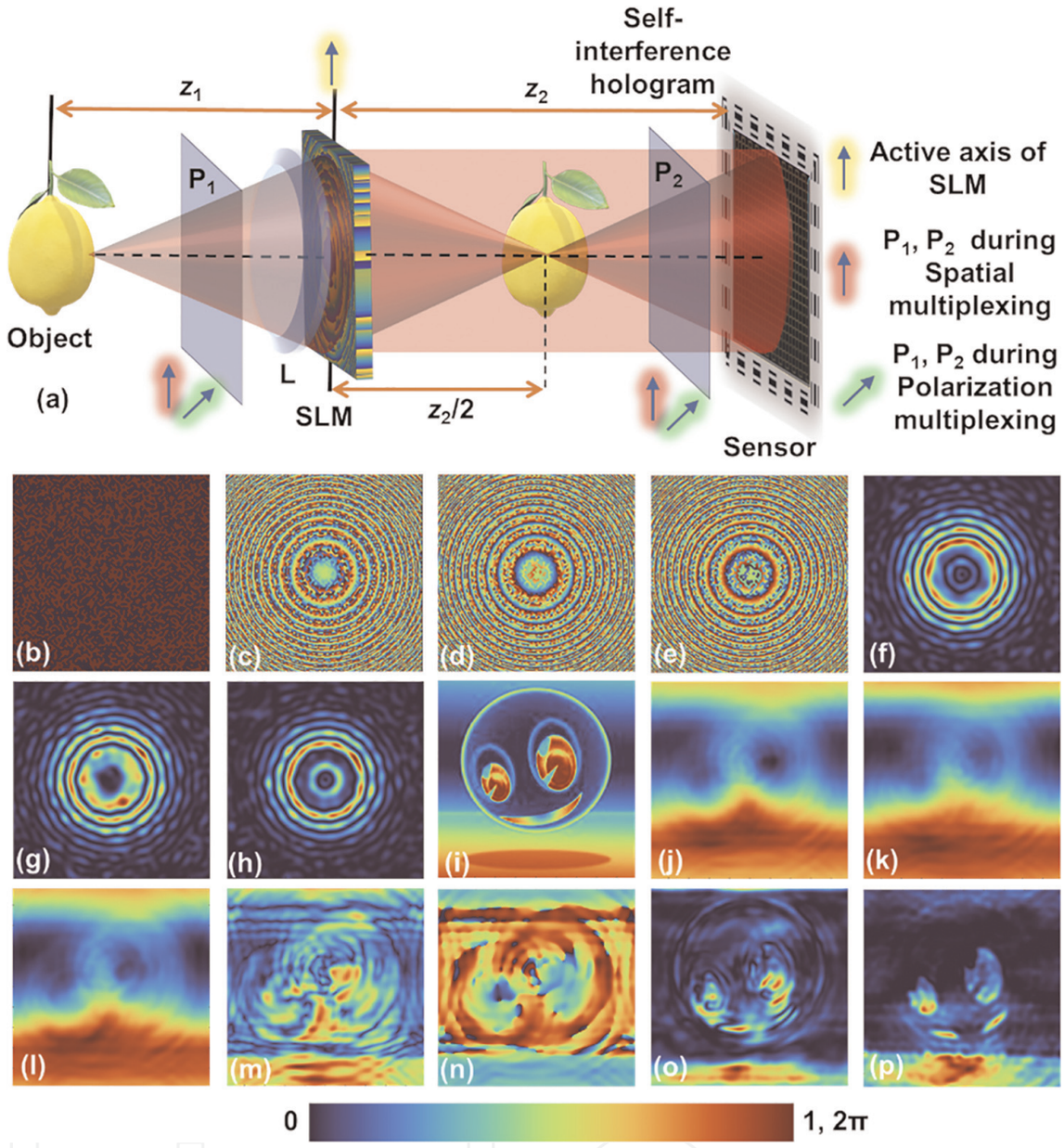

Figure 1.
(a) Optical configuration of FINCH. Two orientations of polarizers P1 and P2 are shown: red for spatial multiplexing and green for polarization multiplexing. The active axis of SLM is shown in yellow. Refractive lens L is not needed in the case of spatial multiplexing. (b) Random multiplexing matrix. Phase images of the randomly multiplexed bifocal lenses with (c) Θ = 0, (d) Θ = 2π/3, and (e) Θ = 4π/3 radians. Simulated PSFs corresponding to (f) Θ = 0, (g) Θ = 2π/3, and (h) Θ = 4π/3 radians. (i) Test object. Holograms simulated for (j) Θ = 0, (k) Θ = 2π/3, and (l) Θ = 4π/3 radians. (m) Amplitude and (n) phase components of the complex hologram. Reconstructed image of the object by (o) numerical backpropagation and (p) NLR (α = 0, β = 0.6).

$Q(b) = e^{j\frac{\pi bR^2}{\lambda}}$,$R = \sqrt{x^2 + y^2}$ and C_1 is a complex constant. The phase function displayed on the SLM is given by $\Phi(x,y) = \left\{\left(\frac{\pi R^2}{\lambda f_1}\right)\right\}_{2\pi} M + \left\{\left(\frac{\pi R^2}{\lambda f_2}\right)\right\}_{2\pi}(1-M)$, where the first function collimates the incoming light when $f_1 = z_1$, while the second function focuses light at $z_2/2$, when $1/f_2 = 1/z_1 + 2/z_2$ and M is a binary random matrix {0,1}. The complex amplitude after the SLM is given as $C_2\sqrt{I_o}Q(1/z_1)e^{-j\Phi(x,y)}$, where C_2 is a complex constant. The self-interference point spread function is given as $I_{\mathrm{PSF}} = \left|C_2\sqrt{I_o}Q(1/z_1)e^{-j\Phi(x,y)} \otimes Q(1/z_2)\right|^2$. The hologram H for an object O can be given as

$I_{PSF} \bigotimes O$, where '$\bigotimes$' is a 2D convolutional operator. At least three holograms H_1, H_2, and H_3 corresponding to Θ = 0, 2π/3, and 4π/3 are recorded, and projected into the complex space as $H_C = H_1\left(e^{-j4\pi/3} - e^{-j2\pi/3}\right) + H_2\left(1 - e^{-j4\pi/3}\right) + H_3\left(e^{-j2\pi/3} - 1\right)$ to form a complex hologram. The image of the object is reconstructed as $I_R = H_C \bigotimes Q\left(\frac{1}{z_R}\right)$, where z_R is the reconstruction distance.

In the above case, FINCH hologram was reconstructed by a numerical backpropagation. Recalling the cases of COACH [27] and I-COACH [28], where there was no real or virtual image plane associated with the optical configuration and the phase masks, the reconstruction was carried out using cross-correlation with prerecorded point spread functions (PSFs). Since FINCH is a linear shift-invariant system, the same approach can be applied to FINCH as well. This idea was tested in 2020, which yielded notable results for FINCH [35, 36]. The past studies with scattering masks revealed that nonlinear reconstruction (NLR) [37] yielded better results than cross-correlation, Lucy−Richardson algorithm (LRA) [38, 39], and regularized filter algorithm [40]. The reconstructed image can be given as $I_R = \left|\mathcal{F}^{-1}\left\{\left|\tilde{I}_{PSF}\right|^{\alpha} exp\left[i\, arg\left(\tilde{I}_{PSF}\right)\right]\left|\tilde{H}\right|^{\beta} exp\left[-i\, arg\left(\tilde{H}\right)\right]\right\}\right|$, where α and β are tuned between -1 and 1, to obtain the minimum entropy given as $-\sum\sum \phi(m,n)\, log\left[\phi(m,n)\right]$, where $\phi(m,n) = |C(m,n)|/\sum_M\sum_N|C(m,n)|$ and (m,n) are the indexes of the correlation matrix, and $C(m,n)$ is the correlation distribution.

A simulation study was carried out using the above equations in MATLAB [41]. The matrix size was 500 × 500 pixels, pixel size Δ = 10 μm, λ = 650 nm, z_1 = 50 cm, z_2 = 1 m, and diameter of optical modulator was 3 mm. The image of the binary random function M used for multiplexing is shown in **Figure 1b**. The phase images for creating three different phase-shifted holograms with Θ = 0, 2π/3, and 4π/3 radians are shown in **Figure 1c–e**, respectively. The PSFs corresponding to **Figure 1c–e** are shown in **Figure 1f–h,** respectively. A test smiley object as shown in **Figure 1i** was used for simulation. The holograms H_1, H_2, and H_3 of the smiley object for Θ = 0, 2π/3 and 4π/3 are shown in **Figure 1j–l**, respectively. The amplitude and phase of H_c are shown in **Figure 1m** and **n,** respectively. The reconstructed image is shown in **Figure 1o**. The reconstruction results using NLR are shown in **Figure 1p**. By comparing **Figure 1o** and **p**, it is seen that the reconstruction using NLR was better. In the evolution of FINCH, the phase-shifting method removed the twin image and bias terms, but the noises associated with the random multiplexing affected the quality of reconstruction.

To avoid the reconstruction noises due to random multiplexing, a polarization multiplexing scheme was introduced [42]. In the first spatial random multiplexing scheme, the light from the object was polarized along the active axis of the SLM, whereas in the polarization multiplexing method, the light from an object was polarized at π/4 radians along the active axis of the SLM. As a result, only about 50% of the incoming light is modulated by the SLM, while the remaining part was not modulated. A second polarizer oriented at π/4 radians along the active axis of the SLM was mounted before the image sensor to create interference between the two object waves. An additional refractive lens was used to collimate the object wave before it is incident on the SLM. In the case of polarization multiplexing scheme, the PSF is given as $I_{PSF} = \left|C_3\sqrt{I_o}Q\left(\frac{1}{z_1}\right)e^{-j\left(\frac{\pi R^2}{\lambda f_1}\right)} \bigotimes Q\left(\frac{1}{z_2}\right) + C_4\sqrt{I_o}Q\left(\frac{1}{z_1}\right)e^{-j\left(\frac{\pi R^2}{\lambda f_2}\right)} \bigotimes Q\left(\frac{1}{z_2}\right)\right|^2$, where C_3 and C_4 are complex constants. The phase images of the mask for Θ = 0, 2π/3 and 4π/3 are

shown in **Figure 2a–c**, respectively. The images of the PSFs for Θ = 0, 2π/3, and 4π/3 are shown in **Figure 2d–f,** respectively and the images of object holograms for Θ = 0, 2π/3, and 4π/3 are shown in **Figure 2g–i,** respectively. The amplitude and phase of the complex hologram formed by projecting **Figure 2g–i** in complex space are shown in **Figure 2j** and **k,** respectively. The reconstructed image of the object is shown in **Figure 2l**. The reconstruction result using NLR is shown in **Figure 2m**.

Recently, a new reconstruction method called Lucy–Richardson–Rosen algorithm (LRRA) was developed by combining the well-known Lucy–Richardson algorithm (LRA) and NLR [43]. In LRA, the $(n+1)^{\text{th}}$ reconstructed image is given as $I_R^{n+1} = I_R^n \left\{ \frac{I_p}{I_R^n \otimes I_{PSF}} \otimes I_{PSF}{}' \right\}$, where $I_{PSF}{}'$ is the complex conjugate of I_{PSF}. This process is iterated until an optimal reconstruction is obtained. The LRA has a forward convolution $I_R^n \otimes I_{PSF}$ and the ratio between this and I_p is correlated with I_{PSF}, which is replaced by the NLR to achieve a better estimation. However, a recent study showed the high sensitivity of LRRA to spatial shifts with a high-resolution image sensor and so may not be suitable for experiments [44]. The reconstruction result (α = 0, β = 0.7, iterations = 10) of LRRA is shown in **Figure 2n** and the direct imaging result is shown in **Figure 2o**.

The above two spatial multiplexing and polarization multiplexing schemes remain the two main configurations of FINCH. Comparing the performances of the above two schemes, it is seen that spatial multiplexing has a higher light throughput than polarization multiplexing while polarization multiplexing has a higher signal-to-noise ratio than spatial multiplexing. As a matter of fact, polarization multiplexing was widely adapted for further developments of FINCH. A secondary multiplexing method was used to reduce the number of camera shots of FINCH from three to one.

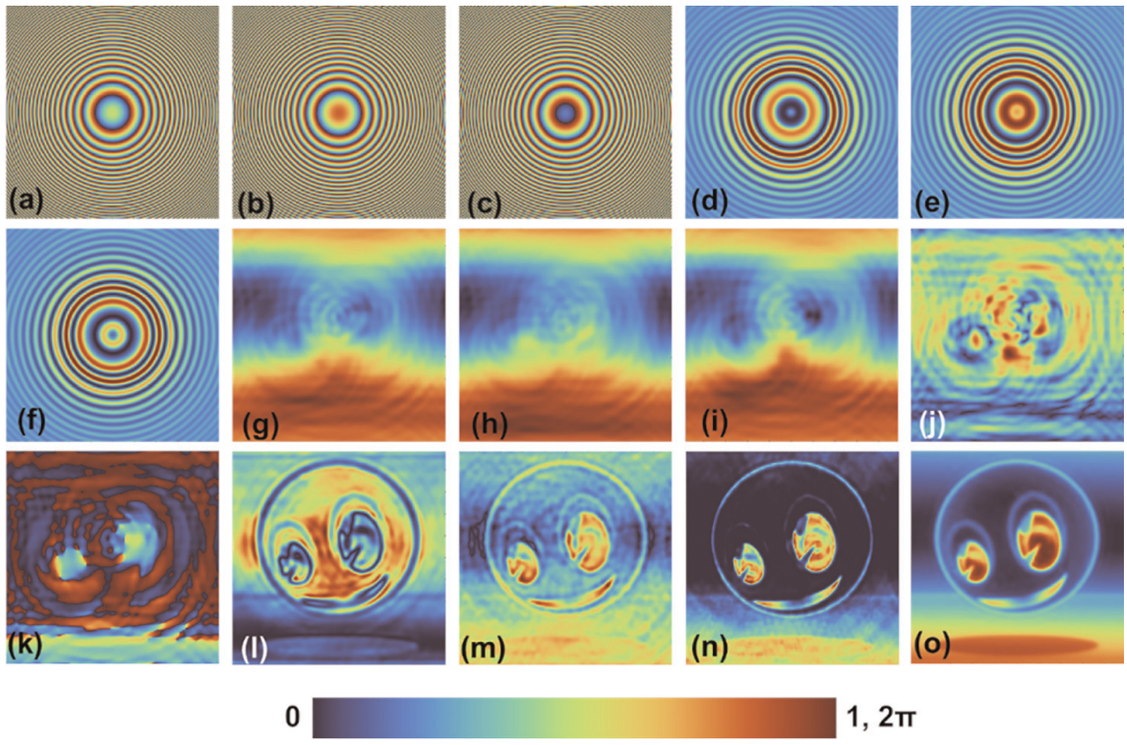

Figure 2.
Phase images of the quadratic phase masks for (a) Θ = 0, (b) Θ = 2π/3, and (c) Θ = 4π/3 radians. PSFs for (d) Θ = 0, (e) Θ = 2π/3, and (f) Θ = 4π/3 radians. Object holograms for (g) Θ = 0, (h) Θ = 2π/3, and (i) Θ = 4π/3 radians. (j) Amplitude and (k) phase of the complex hologram. Reconstruction by (l) numerical backpropagation, (m) nonlinear reconstruction, and (n) Lucy-Richardson-Rosen algorithm. (o) Direct imaging.

In the polarization multiplexing scheme, either spatial multiplexing [45, 46] or a polarization multiplexing with a 4-pol camera [47] was used to record multiple phase-shifted holograms from a single recording. The spatial multiplexing sacrificed the field of view while the polarization multiplexing sacrificed the signal-to-noise ratio. In the above secondary multiplexing schemes, the number of shots required remained the same but it was collected simultaneously distributed in space and polarization states. Recently, a two-step phase-shifting method was developed, which reduced the required number of camera shots in FINCH to two [48]. The evolution of FINCH over the years has been described chronologically in [1, 49].

2.2 Experimental results

To compactify FINCH, from a manufacturing point of view, the spatial multiplexing scheme is easier to realize as the diffractive optical elements involved have features that are super-wavelength. To realize FINCH in polarization multiplexing scheme, metasurfaces with subwavelength features are needed, which will increase the cost of the manufacturing process and often difficult to achieve a large area. As a matter of fact, there have been attempts to realize FINCH in polarization multiplexing scheme using metasurfaces and geometric phase lenses, which resulted in a high cost, low performance, and suffered from low light throughput due to polarizing of the incoming light [50, 51]. At Nanolab of SUT, two different randomly multiplexed diffractive optical elements were designed. The first element consisted of two binary Fresnel zone lenses with focal lengths of 2.5 cm and 5 cm such that the object is at 5 cm and the sensor is at 10 cm from the diffractive element. The second element consisted of a Fresnel zone lens with a focal length of 5 cm and an axicon. The Fresnel zone lenses were designed to include the thickness of glass plate to avoid spherical aberrations [52].

The randomly multiplexed Fresnel zone lenses were manufactured on Indium-Tin-Oxide (ITO)-coated commercial glass plates with a thickness of ∼1 mm, index of refraction of ∼1.5, and a high transmittivity (>95%). The substrate was cleaned in an ultrasonic bath in acetone and iso-propyl alcohol (IPA) for 10 minutes and baked on a hotplate at 180°C for 5 minutes to remove the residual solvents. When the substrate was cooled to room temperature, it was spin-coated with PMMA 950K A7 positive resist at 2000 RPM for a minute to achieve a resist thickness of λ. During spin coating, an edge of the substrate was masked with a tape, which was removed after spin coating. This masked area was connected to the metal clip of substrate holder in the electron beam lithography system RAITH150^{TWO}. An acceleration voltage of 10kV, aperture of 120 μm, and a beam current of ∼3 nA was used with a working distance of 10 mm and write field of 100 μm. The diffractive element designed with a diameter of 5 mm was fabricated (∼6 hours) without any stitching errors. The fabricated device was developed in methyl isobutyl ketone (MIBK) and IPA in the ratio of 1:3 for 1 minute. The optical microscope image of the randomly multiplexed Fresnel zone lenses is shown in **Figure 3a**. A second diffractive element consisting of a Fresnel zone lens and an axicon with a period of 100 μm was fabricated under the same fabrication conditions. The optical microscope image of the fabricated device is shown in **Figure 3b**. The magnified sections of the 3(a) and 3(b) are shown in **Figure 3c** and **d,** respectively.

Optical experiments were carried out using the fabricated devices and a spatially incoherent source (Thorlabs, M617L3, λ_c = 617 nm, FWHM = 18 nm). The diffractive element was located at 5 cm from the object and the sensor (Thorlabs DCU223M, 1024

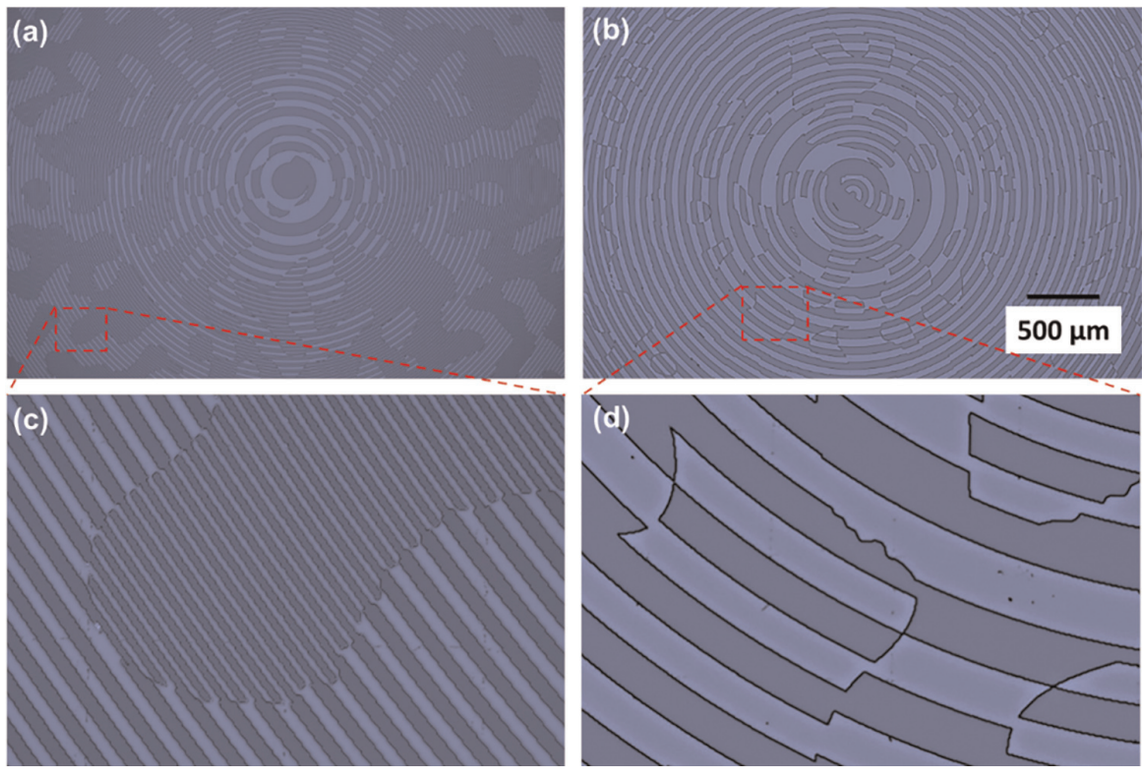

Figure 3.
Optical microscope images of randomly multiplexed (a) Fresnel zone lenses and (b) Fresnel zone lens and axicon. Magnified images of sections of (a) and (b) are shown in (c) and (d), respectively.

× 768 pixels, pixel size = 4.65 µm) was located at 10 cm from the diffractive lens. In the first experiment, the randomly multiplexed Fresnel zone lenses were mounted. In the first step, the PSF was recorded using a pinhole with a diameter of 20 µm as shown in **Figure 4a**. The element 1 of Group 4 (16 lp/mm, grating period = 62.5 µm) of the United States Air Force (USAF) resolution target replaced the pinhole in the next step. The direct imaging result recorded at a distance of 5 cm from the diffractive element is shown in **Figure 4b**. The image of the recorded object hologram at 10 cm from the diffractive element is shown in **Figure 4c**. The reconstruction result using NLR (α = 0.2, β = 0.6) is shown in **Figure 4d**. The experiment was repeated to image a dragonfly larva wing, whose hologram is shown in **Figure 4e**. The reconstruction result and direct imaging result are shown in **Figure 4f** and **g,** respectively. The biological sample was reconstructed using PSFs recorded at different depths of the wing. The computational refocusing at different planes of the sample is shown in **Figure 4h**.

The experiment was repeated using the second diffractive element – randomly multiplexed Fresnel zone lens and axicon. The PSFs recorded for λ = 617 nm and λ = 530 nm are shown in **Figure 5a** and **b,** respectively. Two objects (Group – 2, Element – 6, 7.13 *lp/mm*) of USAF and National Bureau of Standards (NBS) resolution target (7.1 *lp/mm*) were mounted one after the other, and their holograms were captured and summed as shown in **Figure 5c**. The reconstructed results of USAF and NBS objects using the corresponding PSFs are shown in **Figure 5d** and **e,** respectively.

2.3 Discussion

FINCH has been implemented in a compact optical configuration using static diffractive optical elements manufactured using electron beam lithography

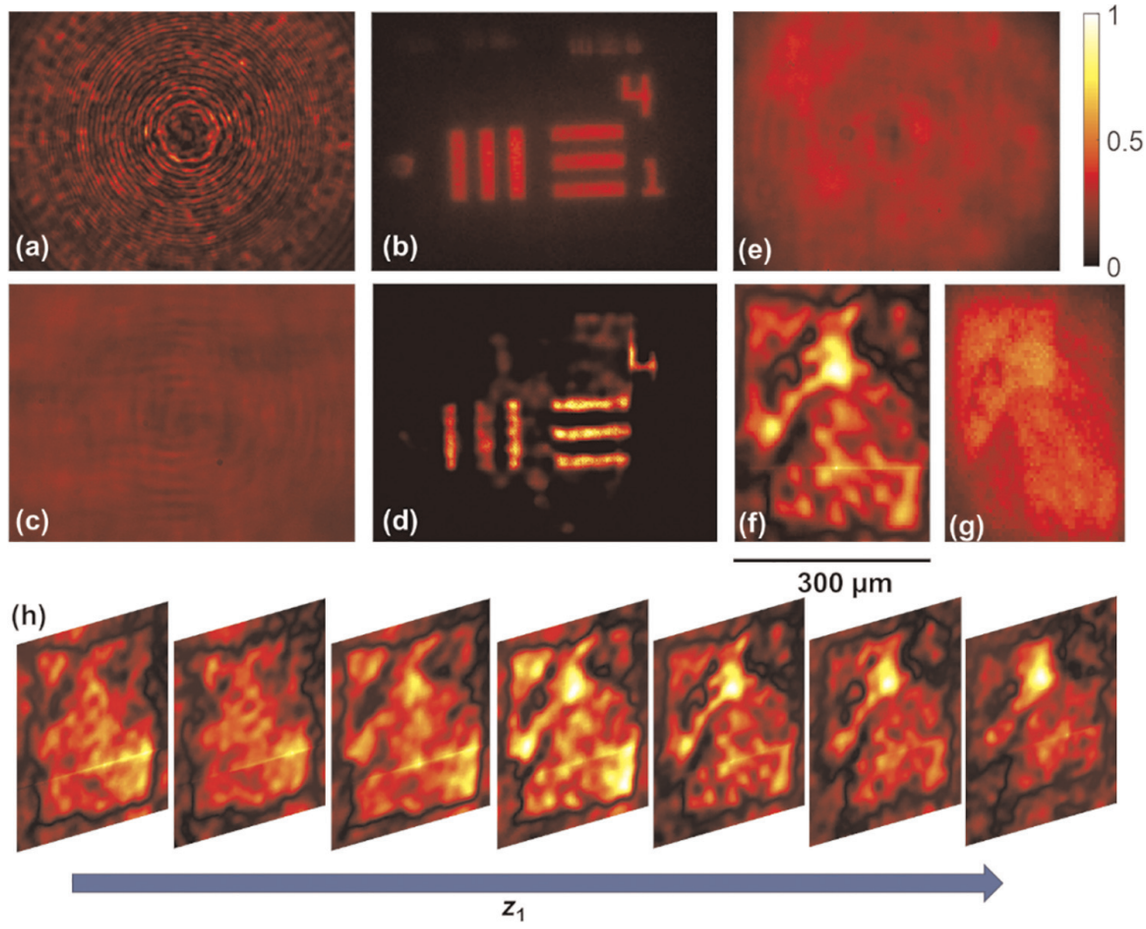

Figure 4.
(a) PSF. (b) Direct imaging result recorded at the focal plane of one of the Fresnel zone lenses, (c) object hologram and (d) reconstruction result for randomly multiplexed Fresnel zone lenses. (e) Hologram of a section of dragonfly larvae wing. (f) Reconstruction result using NLR (α = 0, β = 0.58) and (g) direct imaging result. (h) Results of 3D computational refocusing.

techniques. The imaging distances were only 5 cm between object to diffractive element and 10 cm between diffractive element and sensor, which is close to palm-size systems [53]. The diffraction efficiency was about 40%, which is higher than polarization multiplexing configurations. Both 3D spatial and spectral imaging have been demonstrated. The preliminary results are promising.

3. Interferenceless-coded aperture correlation holography (I-COACH)

3.1 Methodology and simulation results

The optical configuration of I-COACH or CAI is simpler than FINCH, as shown in **Figure 6,** consisting of only one optical element between the object and image sensor. In this study, only chaotic coded apertures are considered [54]. The use of URA [21], MURA [22], and masks for spectral imaging methods involve many optical components [23] unlike I-COACH with chaotic coded apertures. The intensity distribution for an object O is given as $I_O = I_{PSF} \otimes O$ and the reconstructed image is given as $I_R = I_O * I_{PSF} = I_{PSF} * I_{PSF} \otimes O$, where '$*$' is a 2D correlation operator. The above cross-correlation procedure is not optimal and NLR is the currently known best reconstruction method. So, the above procedure will be implemented using NLR. The simulation

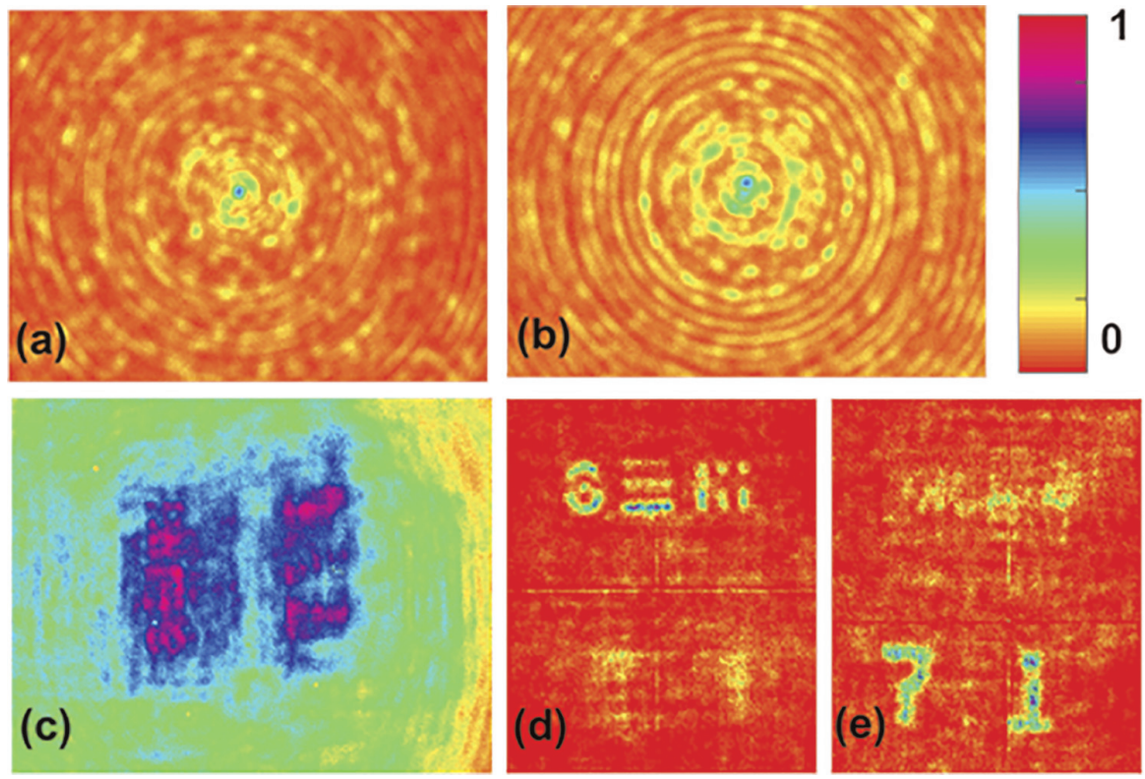

Figure 5.
PSFs recorded for (a) λ = 617 nm and (b) 530 nm. Holograms of USAF and NBS illuminated by λ = 617 nm and λ = 530 nm, respectively, but mounted at the same distance of 5 cm. The reconstruction results using NLR (α = 0, β = 0.63), (d) PSF (λ = 617 nm), and (e) PSF (λ = 530 nm).

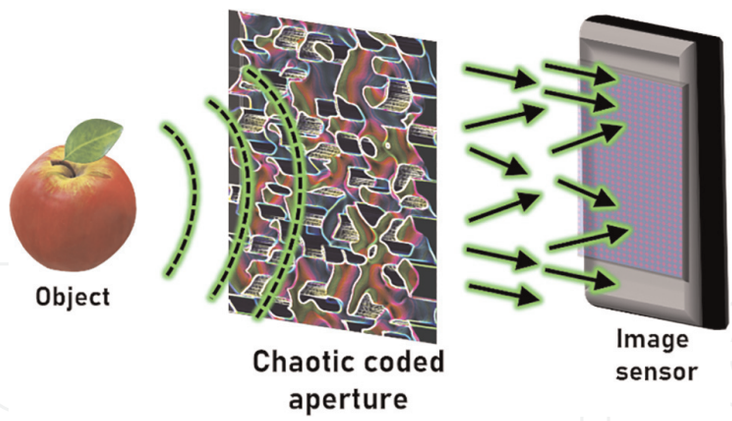

Figure 6.
Optical configuration of I-COACH or CAI with chaotic coded aperture.

conditions were as described in Section 2 with the object distance at 50 cm from the diffractive element, and the distance between the diffractive element and the image sensor is 1 m. The images of an amplitude type mask with a fill factor of 0.5 and chaotic coded aperture phase masks with scattering ratios σ = 1, 0.5, 0.2, 0.1, and 0.02 are shown in the first row of **Figure 7**. The simulated PSFs, object intensity distributions, and reconstruction results of the test object using NLR are shown in the second, third, and fourth rows, respectively.

The amplitude mask was designed by rounding off a normalized (0,1) 2D random function. The phase masks were engineered using Gerchberg–Saxton algorithm [55] by imposing a constraint on the size of the window in the spectrum domain as

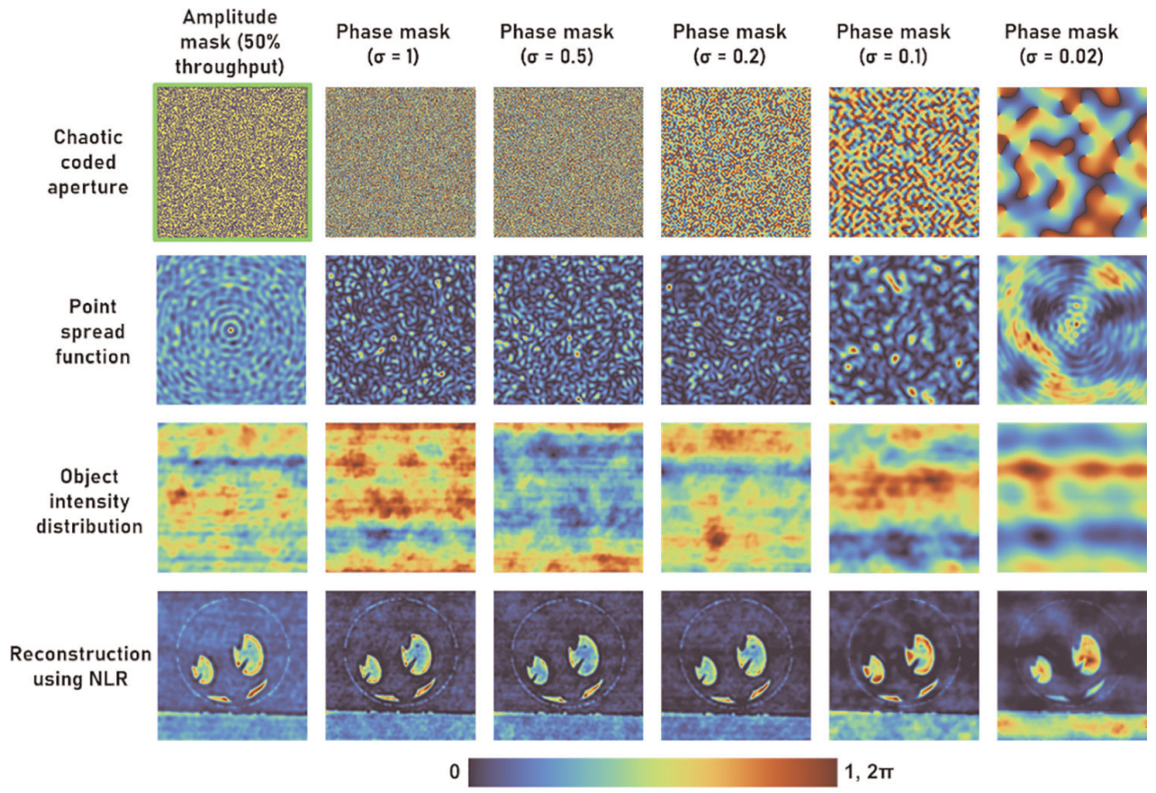

Figure 7.
Simulation results of PSF, object intensity distribution and reconstruction results using NLR for an amplitude mask with 50% light throughput (green window), phase masks with σ = 1, 0.5, 0.2, 0.1, and 0.02.

discussed in [54], where $\sigma = p/P$, where P is the size of the matrix and p is the size of the window. The speckle sizes decrease with an increase in the scattering degree and consequently, the resolution of the reconstruction improves with an increase in the scattering degree. The reconstruction result of the amplitude mask had a similar resolution as that of the phase mask with maximum scattering degree but additional background noise. In addition to the above, there are other scattering masks that generate a random array of points [56] and ring patterns [57], but multiplane imaging requires a multiplexing approach.

3.2 Experimental results

The chaotic coded apertures were realized as a pinhole array [58, 59] as well as a quasi-random phase mask manufactured using lithography procedures [60]. It must be noted that the first demonstrations of I-COACH without lens required an SLM as at least two camera shots were needed in order to create a bipolar matrix [28, 61]. Due to the expected background noise in amplitude masks, the pinhole array mask was designed using a two-step optimization procedure. The number of pinholes was selected as 2000. In the first step, the 2000 pinholes were spatially randomly arranged in 1000 ways and the reconstruction noise was simulated for every case. The optimal case of random arrangement was selected for the next round of optimization. In the next step, the location of every pinhole was shifted in steps of 5 pixels every time the background noise was estimated. When the noise decreased, the new position was retained and if the noise increased, the pinhole was shifted back to the previous position. The above two optimization procedures involved a total of about 5000 iterations. The final mask pattern demonstrated an SNR improvement of ~60% in

comparison to a case with a minimum SNR. The final mask design was transferred to a chromium-coated mask plate using Intelligent micropatterning SF100 XPRESS. The size of the QRAP was 8 mm and the diameter of the pinholes was 80 μm after fabrication.

The PSF was recorded using a pinhole of diameter of 20 μm for an object distance of 10 cm from the pinhole array and sensor at 10 cm from the pinhole array as shown in **Figure 8a**. The pinhole was replaced by a USAF object (Group 2, Elements 4, 5, and 6) and the intensity distribution was recorded as shown in **Figure 8b**. The reconstruction result using NLR for ($\alpha = 0$, $\beta = 0.6$) is shown in **Figure 8c**. The experiment was repeated for a section of wing of an insect. The PSF and object intensity distributions are shown in **Figure 8d** and **e,** respectively. The reconstructed image is shown in **Figure 8f**. The experiment was repeated to record the 5D information along x, y, z, λ, and t. A spark was generated by creating an electrical discharge and the light was modulated by the pinhole array mask and the intensity distribution was recorded. A high-speed camera (Phantom v2512, monochrome, 800×1280, $\Delta = 28\,\mu m$) was used for recording the event. The intensity distribution at times $t = 0$, 80, and 160 μs are shown in **Figure 9a**, **d,** and **g,** respectively, which were reconstructed using green and red PSFs using NLR, and the reconstructed images for green wavelength at times $t = 0$, 80, and 160 μs are shown in **Figure 9b**, **e** and **f**, respectively. The reconstructed images for red wavelength at times $t = 0$, 80, and 160 μs are shown in **Figure 9c, f,** and **i,** respectively. The object intensity pattern was reconstructed using PSFs synthesized for different depths using the scaling approach and tomography of the spark pattern at time $t = 0$ was generated as shown in **Figure 9j**.

In the experiments using pinhole array, the results were significant, but the main challenge was the low light throughput. The above mask could not be used for imaging in low-intensity conditions such as fluorescence and astronomical imaging. To expand the applicability of the method, improvement to design was made at multiple levels. In the first step, the amplitude mask was replaced by a phase mask. A ground glass diffuser is a good choice but offers less control over the intensity distribution [62–64].

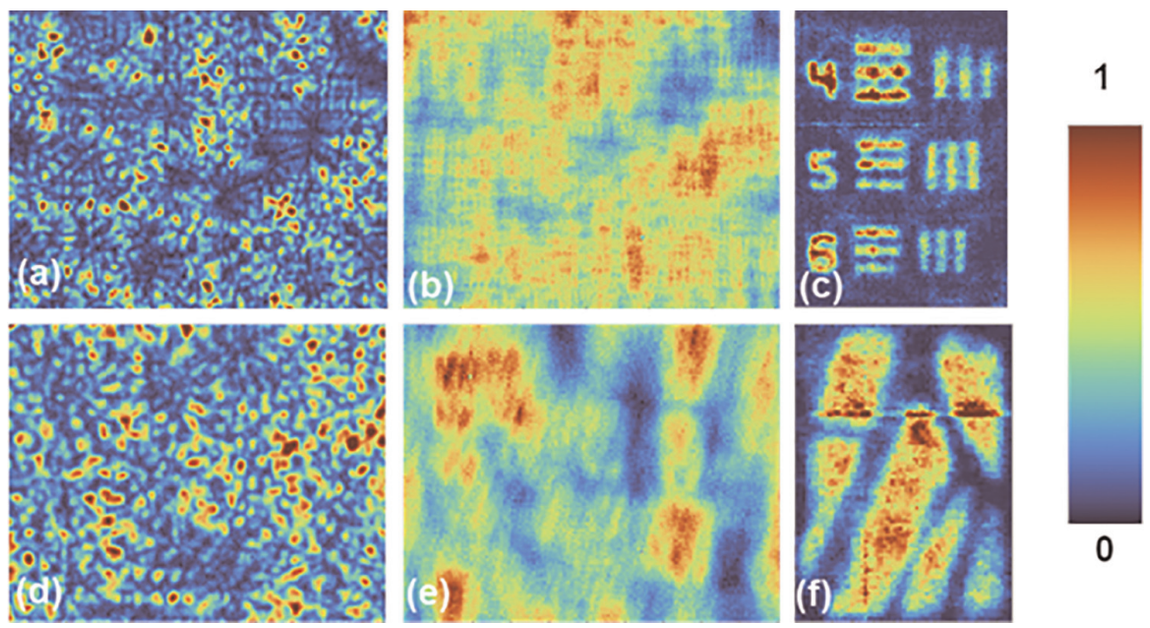

Figure 8.
Images of the (a) PSF and (b) object intensity distribution for USAF object, and (c) reconstruction result by NLR. (d) PSF and (e) object intensity distribution for wing of an insect, and (f) reconstruction result by NLR.

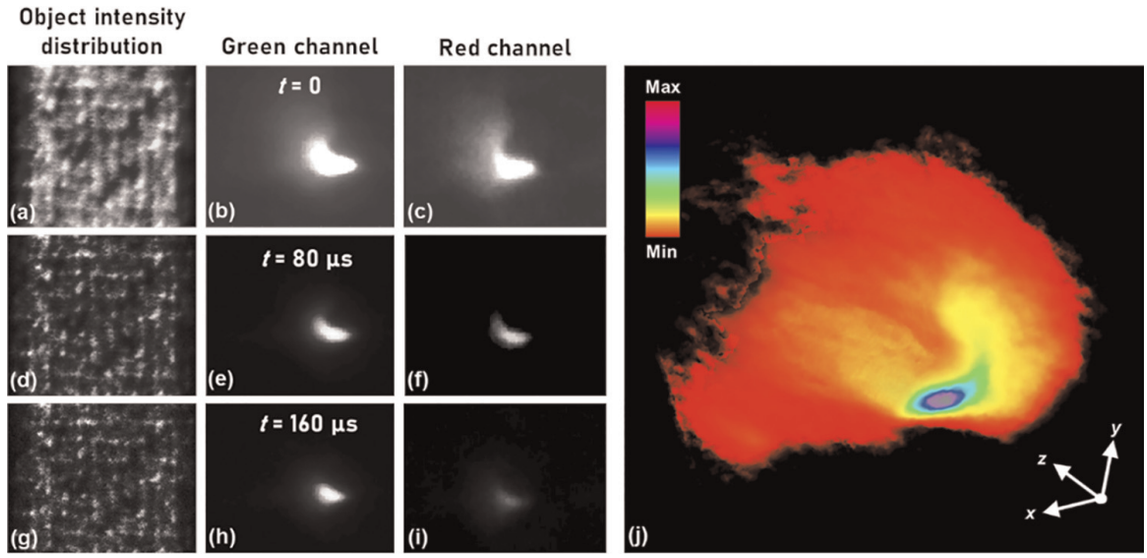

Figure 9.
(a) Recorded object intensity pattern and reconstruction result for (b) green channel and (c) red channel at t = 0. *(d) Recorded object intensity pattern and reconstruction result for (e) green channel and (f) red channel at* t = 80 *µs. (g) Recorded object intensity pattern and reconstruction result for (h) green channel and (i) red channel at* t = 160 *µs. (j) Tomography of the spark pattern.*

So, the phase mask was designed in a specific way by combining a chaotic coded phase mask and a quadratic phase function. The resulting phase function is called a quasi-random lens (QRL). This special lens behaves like a Fresnel zone lens, but instead of collecting light and focusing it on a point, it focuses on an area and within the area, light is scattered. In other words, the QRL creates controlled scattering similar to the mask designed in lensless I-COACH [61]. The generated phase of the QRL was converted into two levels by a standard rounding-off procedure. A QRL with a diameter of 5 mm and focal length of 5 cm was fabricated using electron beam lithography (RAITH150^{TWO}) using the same fabrication settings as described in Section 2. The optical microscope image of the fabricated device is shown in **Figure 10a**. The PSFs recorded using a pinhole with a diameter of 100 µm and using red (617 nm) and green wavelengths (530 nm) as shown in **Figure 10b** and **c,** respectively. The object hologram obtained by summing of the object intensity distributions recorded for two objects NBS (10 lp/mm) and USAF (Group 2, Element 2) separated by 1 cm and

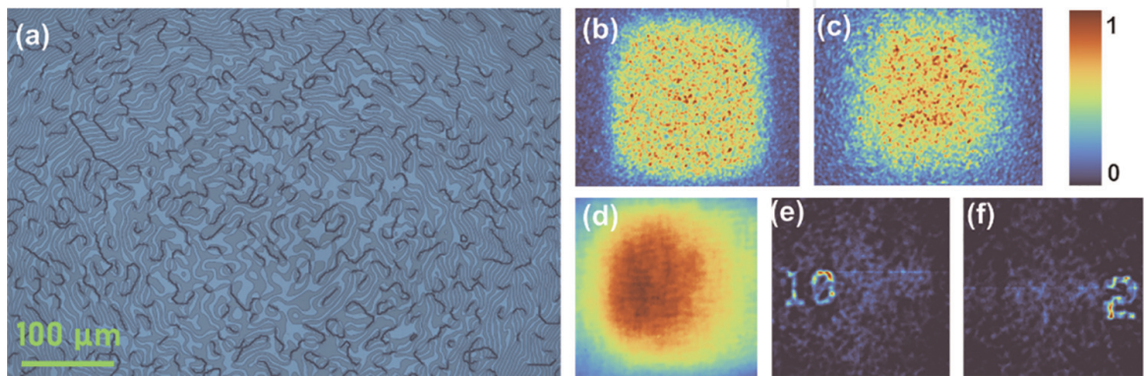

Figure 10.
(a) Optical microscope image of the QRL. Recorded PSFs for (b) 617 nm and (c) 530 nm. (d) Object hologram. Reconstruction results using PSFs recorded using (e) red and (f) green LEDs.

illuminated by red and green wavelengths, respectively, is shown in **Figure 10d**. The reconstruction results using NLR and red and green PSFs are shown in **Figure 10e** and **f,** respectively.

3.3 Discussion

I-COACH has been realized in a compact optical configuration with a total length of 20 cm. This is quite compact in comparison to CASSI, MURA, and also other incoherent holography techniques. The maximum efficiency achievable with the binary QRL is only about 40%, which can be improved to >90% by manufacturing a greyscale version of the QRL. With the latest advancements in rapid fabrication technologies and nanoimprint techniques, mass production of greyscale QRL is not expensive in comparison to using active devices such as SLM [65–68].

4. Optical tweezer perspectives inspired by FINCH configuration

Optical Tweezer (OT) is a powerful tool to manipulate micron-sized objects by creating an optical trap [69, 70]. In 1970, Arthur Ashkin first reported that the gradient forces from the laser can trap micron-sized particles [71]. Years later, Ashkin and his colleagues invented optical tweezers and demonstrated the ability of the single-beam optical trap to attract particles intended for analysis [72]. The advancements in the technologies such as invention of SLMs and diffractive optical elements led to the development of holographic optical tweezers (HOT) [73]. In general, a conventional tweezer system comprises trapping architecture and imaging architecture as shown in **Figure 11**. In HOT, computer-generated holograms (CGH) are designed and displayed in the SLM to modulate the trapping beam for sample control and manipulation. The trapping beam can be single or multiple based on the design adapted in the CGH and can be dynamically manipulated. The HOT quickly emerged and became indispensable in the field of biology [74–76].

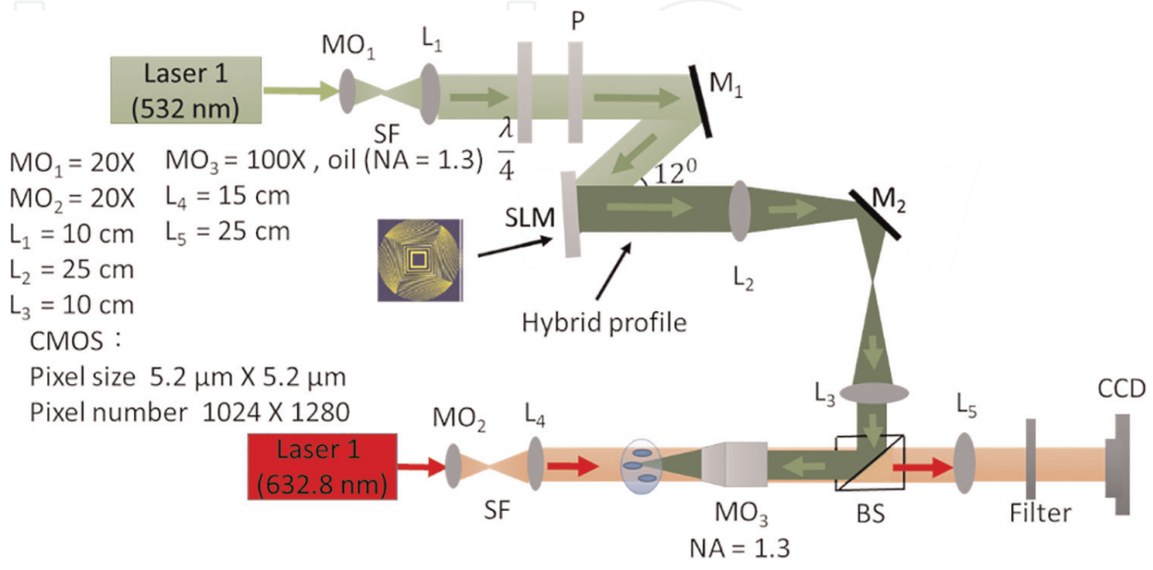

Figure 11.
Schematic of the typical holographic optical tweezer. Red and green represent the trapping and the imaging system architectures.

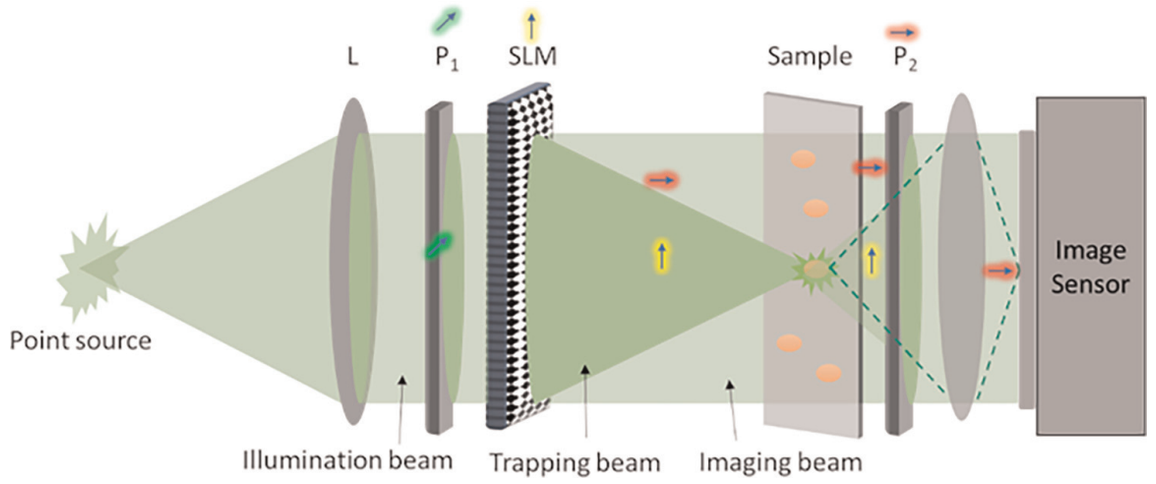

Figure 12.
Optical trapping and imaging configuration inspired for FINCH's polarization multiplexing scheme.

An alternate architecture inspired by FINCH polarization multiplexing scheme to the conventional trapping architecture for single beam compact trapping and imaging is shown in **Figure 12**. The proposed optical configuration uses a polarization multiplexing scheme. A polarizer P_1 at 45° orientation with respect to the active axis of the SLM was set before the SLM and a diffractive lens is displayed on the SLM. At the SLM, only part of the optical beam is modulated and so two beams namely, trapping beam and imaging beam, are generated. The modulated trapping beam creates a tightly focused spot to trap the sample and the unmodulated imaging beam is utilized for the imaging. Before the image sensor, a second polarizer P_2 oriented at 90° with respect to the active axis of the SLM was introduced to avoid the trapping beam, affecting the imaging. The optical power of the trapping beam can be controlled by adjusting the polarization degree of P_1. To achieve tight focusing, a projection system might be needed, which can increase the strength of the trap and imaging beams.

5. Summary and conclusion

In this chapter, two widely used incoherent holography systems, namely FINCH and I-COACH, are discussed with a focus on compactification using static diffractive optical elements. In FINCH, the required three camera shots and active optical device have been avoided by applying NLR. The diffractive optical element proposed in the first version of FINCH was designed and fabricated using electron beam lithography techniques in a compact optical configuration of 15 cm. I-COACH was realized using both an amplitude element and a phase element fabricated using photolithography and electron beam lithography systems, respectively, in a compact 20 cm configuration. The preliminary results are promising to begin research on building prototypes. There are still some challenges present in FINCH, as well as in I-COACH. From the manufacturing side, it is necessary to fabricate multilevel structures to improve the efficiency from the current 40% to >90%, which increases the cost and time of fabrication. With the latest developments in Femtosecond fabrication methods, it is possible to rapidly manufacture high-efficiency diffractive optical elements at a low cost [77–79]. The second challenge lies in the current performances of computational reconstruction methods. In both FINCH and I-COACH, the computational

reconstruction generated background noise that could not be minimized to the level of lens-based imaging. With the advancements in deep learning techniques, we believe that it is possible to achieve a high SNR. The chapter concludes with an intriguing possibility of extending FINCH configuration for optical trapping experiments, which we believe may revolutionize optical tweezer and tomography research directions.

Acknowledgements

V.A thanks Tiia Lillemaa and Aravind Simon for their administrative support. D. S.; S. H. N.; T. K.; and S. J. are grateful for the financial support via ARC Linkage LP190100505 project. V. A. acknowledges the European Union's Horizon 2020 Research and Innovation Programme grant agreement No. 857627 (CIPHR). V.B.; P.J.M.; C.D. acknowledges King Abdullah University of Science and Technology (KAUST) for the funding.

Conflict of interest

Christian Depeursinge has financial interests in Lyncee Tec and Nanolive; Pierre J Magistretti has financial interests in Lyncee Tec.

Author details

Vijayakumar Anand[1*], Soon Hock Ng[2], Tomas Katkus[2], Daniel Smith[2], Vinoth Balasubramani[3], Denver P. Linklater[4], Pierre J. Magistretti[3], Christian Depeursinge[3], Elena P. Ivanova[4] and Saulius Juodkazis[2]

1 Institute of Physics, University of Tartu, Tartu, Estonia

2 Optical Sciences Centre, Swinburne University of Technology, Melbourne, Australia

3 Division of Biological and Environmental Sciences and Engineering, King Abdullah University of Science and Technology (KAUST), Saudi Arabia

4 School of Science, STEM College, RMIT University, Melbourne, Australia

*Address all correspondence to: vijayakumar.anand@ut.ee

References

[1] Rosen J, Vijayakumar A, Kumar M, Rai MR, Kelner R, Kashter Y, et al. Recent advances in self-interference incoherent digital holography. Advances in Optics and Photonics. 2019;**11**:1-66. DOI: 10.1364/AOP.11.000001

[2] Gabor D. Progress in holography. Reports on Progress in Physics. 1969;**32**: 395-404. DOI: 10.1088/0034-4885/32/1/308

[3] Osten W, Faridian A, Gao P, Körner K, Naik D, Pedrini G, et al. Recent advances in digital holography. Applied Optics. 2014;**53**:G44-G63. DOI: 10.1364/AO.53.000G44

[4] Goodman JW. Introduction to Fourier Optics. Englewood, Colorado: Roberts & Co.; 2005

[5] Roddier C, Roddier F, Demarcq J. Compact rotational shearing interferometer for astronomical applications. Optical Engineering. 1989; **28**:280166. DOI: 10.1117/12.7976903

[6] Cochran G. New method of making Fresnel transforms with incoherent light. JOSA. 1966;**56**:1513-1517. DOI: 10.1364/JOSA.56.001513

[7] Sirat G, Psaltis D. Conoscopic holography. Optics Letters. 1985;**10**:4-6. DOI: 10.1364/OL.10.000004

[8] Rosen J, Brooker G. Digital spatially incoherent Fresnel holography. Optics Letters. 2007;**32**:912-914. DOI: 10.1364/OL.32.000912

[9] Kelner R, Rosen J. Spatially incoherent single channel digital Fourier holography. Optics Letters. 2012;**37**: 3723-3725. DOI: 10.1364/OL.37.003723

[10] Hong J, Kim MK. Single-shot self-interference incoherent digital holography using off-axis configuration. Optics Letters. 2013;**38**:5196-5199. DOI: 10.1364/OL.38.005196

[11] Rosen J, Brooker G. Non-scanning motionless fluorescence three-dimensional holographic microscopy. Nature Photonics. 2008;**2**:190-195. DOI: 10.1038/nphoton.2007.300

[12] Wu P, Zhang D, Yuan J, Zeng S, Gong H, Luo Q, et al. Large depth-of-field fluorescence microscopy based on deep learning supported by Fresnel incoherent correlation holography. Optics Express. 2022;**30**:5177-5191. DOI: 10.1364/OE.451409

[13] Bu Y, Wang X, Li Y, Du Y, Gong Q, Zheng G, et al. Tunable edge enhancement by higher-order spiral Fresnel incoherent correlation holography system. Journal of Physics D: Applied Physics. 2021;**54**:125103. DOI: 10.1088/1361-6463

[14] Kashter Y, Vijayakumar A, Miyamoto Y, Rosen J. Enhanced super resolution using Fresnel incoherent correlation holography with structured illumination. Optics Letters. 2016;**41**: 1558-1561. DOI: 10.1364/OL.41.001558

[15] Anand V, Rosen J, Ng SH, Katkus T, Linklater DP, Ivanova EP, et al. Edge and contrast enhancement using spatially incoherent correlation holography techniques. Photonics. 2021;**8**:224. DOI: 10.3390/photonics8060224

[16] Siegel N, Brooker G. Single shot holographic super-resolution microscopy. Optics Express. 2021;**29**: 15953-15968. DOI: 10.1364/OE.424175

[17] Liang J. Punching holes in light: Recent progress in single-shot coded-

aperture optical imaging. Reports on Progress in Physics. 2020;**83**:116101. DOI: 10.1088/1361-6633/abaf43

[18] Caroli E, Stephen JB, Di Cocco G, Natalucci L, Spizzichino A. Coded aperture imaging in X-and gamma-ray astronomy. Space Science Reviews. 1987; **45**:349-403. DOI: 10.1007/BF00171998

[19] Ables JG. Fourier transform photography: A new method for X-ray astronomy. Publications of the Astronomical Society of Australia. 1968; **1**:172-173. DOI: 10.1017/S1323358000011292

[20] Dicke RH. Scatter-hole cameras for x-rays and gamma rays. The Astrophysical Journal. 1968;**153**:L101-L106. DOI: 10.1086/180230

[21] Fenimore EE, Cannon TM. Uniformly redundant arrays: Digital reconstruction methods. Applied Optics. 1981;**20**:1858-1864. DOI: 10.1364/AO.20.001858

[22] Olmos P, Cid C, Bru A, Oller JC, de Pablos JL, Perez JM. Design of a modified uniform redundant-array mask for portable gamma cameras. Applied Optics. 1992;**31**:4742-4750. DOI: 10.1364/AO.31.004742

[23] Wagadarikar A, John R, Willett R, Brady D. Single disperser design for coded aperture snapshot spectral imaging. Applied Optics. 2008;**47**:B44-B51. DOI: 10.1364/AO.47.000B44

[24] Kittle D, Choi K, Wagadarikar A, Brady DJ. Multiframe image estimation for coded aperture snapshot spectral imagers. Applied Optics. 2010;**49**: 6824-6833. DOI: 10.1364/AO.49.006824

[25] Arce GR, Brady DJ, Carin L, Arguello H, Kittle DS. Compressive coded aperture spectral imaging: An introduction. IEEE Signal Processing Magazine. 2013;**31**:105-115. DOI: 10.1109/MSP.2013.2278763

[26] Chi W, George N. Optical imaging with phase-coded aperture. Optics Express. 2011;**19**:4294-4300. DOI: 10.1364/OE.19.004294

[27] Vijayakumar A, Kashter Y, Kelner R, Rosen J. Coded aperture correlation holography–a new type of incoherent digital holograms. Optics Express. 2016; **24**:12430-12441. DOI: 10.1364/OE.24.012430

[28] Vijayakumar A, Rosen J. Interferenceless coded aperture correlation holography–a new technique for recording incoherent digital holograms without two-wave interference. Optics Express. 2017;**25**: 13883-11396. DOI: 10.1364/OE.25.013883

[29] Rai MR, Vijayakumar A, Ogura Y, Rosen J. Resolution enhancement in nonlinear interferenceless COACH with point response of subdiffraction limit patterns. Optics Express. 2019;**27**: 391-403. DOI: 10.1364/OE.27.000391

[30] Malinauskas M, Žukauskas A, Hasegawa S, Hayasaki Y, Mizeikis V, Buividas R, et al. Ultrafast laser processing of materials: From science to industry. Light: Science & Applications. 2016;**5**:e16133. DOI: 10.1038/lsa.2016.133

[31] Marcinkevičius A, Juodkazis S, Watanabe M, Miwa M, Matsuo S, Misawa H, et al. Femtosecond laser-assisted three-dimensional microfabrication in silica. Optics Letters. 2001;**26**:277-279. DOI: 10.1364/OL.26.000277

[32] Matsuo S, Juodkazis S, Misawa H. Femtosecond laser microfabrication of periodic structures using a microlens

array. Applied Physics A. 2005;**80**: 683-685. DOI: 10.1007/s00339-004-3108-x

[33] Juodkazis S, Rosa L, Bauerdick S, Peto L, El-Ganainy R, John S. Sculpturing of photonic crystals by ion beam lithography: Towards complete photonic bandgap at visible wavelengths. Optics Express. 2011; **19**:5802-5810. DOI: 10.1364/OE.19.005802

[34] Juodkazis S, Yamaguchi A, Ishii H, Matsuo S, Takagi H, Misawa H. Photo-electrochemical deposition of platinum on TiO_2 with resolution of twenty nanometers using a mask elaborated with electron-beam lithography. Japanese Journal of Applied Physics. 2001;**40**:4246. DOI: 10.1143/JJAP.40.4246

[35] Vijayakumar A, Katkus T, Lundgaard S, Linklater DP, Ivanova EP, Ng SH, et al. Fresnel incoherent correlation holography with single camera shot. Opto-Electronic Advances. 2020;**3**:08200004. DOI: 10.29026/oea.2020.200004

[36] Anand V, Katkus T, Juodkazis S. Randomly multiplexed diffractive lens and axicon for spatial and spectral imaging. Micromachines. 2020;**11**:437. DOI: 10.3390/mi11040437

[37] Rai MR, Vijayakumar A, Rosen J. Non-linear adaptive three-dimensional imaging with interferenceless coded aperture correlation holography (I-COACH). Optics Express. 2018;**26**: 18143-18154. DOI: 10.1364/OE.26.018143

[38] Richardson WH. Bayesian-based iterative method of image restoration. JoSA. 1972;**62**:55-59. DOI: 10.1364/JOSA.62.000055

[39] Lucy LB. An iterative technique for the rectification of observed distributions. The Astronomical Journal. 1974;**79**:745. DOI: 10.1086/111605

[40] Ng SH, Anand V, Katkus T, Juodkazis S. Invasive and non-invasive observation of occluded fast transient events: Computational tools. Photonics. 2021;**8**:253. DOI: 10.3390/photonics 8070253

[41] Bhattacharya S, Vijayakumar A. Design and Fabrication Of Diffractive Optical Elements with MATLAB. Bellingham, Washington, USA: SPIE Press; 2017. DOI: 10.1117/3.2261461

[42] Rosen J, Siegel N, Brooker G. Theoretical and experimental demonstration of resolution beyond the Rayleigh limit by FINCH fluorescence microscopic imaging. Optics Express. 2011;**19**:26249-26268. DOI: 10.1364/OE.19.026249

[43] Vijayakumar A, Molong H, Jovan M, Hock NS, Tomas K, Annaleise K, et al. Single-shot mid-infrared incoherent holography using Lucy-Richardson-Rosen algorithm. Opto-Electronic Science. 2022;**1**:210006. DOI: 10.29026/oes.2022.210006

[44] Anand V, Khonina S, Kumar R, Dubey N, Reddy AN, Rosen J, et al. Three-dimensional incoherent imaging using spiral rotating point spread functions created by double-helix beams. Nanoscale Research Letters. 2022;**17**:1-3. DOI: 10.1186/s11671-022-03676-6

[45] Sakamaki S, Yoneda N, Nomura T. Single-shot in-line Fresnel incoherent holography using a dual-focus checkerboard lens. Applied Optics. 2020; **59**:6612-6618. DOI: 10.1364/AO.393176

[46] Nobukawa T, Muroi T, Katano Y, Kinoshita N, Ishii N. Single-shot phase-

shifting incoherent digital holography with multiplexed checkerboard phase gratings. Optics Letters. 2018;**43**: 1698-1701. DOI: 10.1364/OL.43.001698

[47] Tahara T, Kanno T, Arai Y, Ozawa T. Single-shot phase-shifting incoherent digital holography. Journal of Optics. 2017;**19**:065705. DOI: 10.1088/2040-8986/aa6e82

[48] Tahara T, Kozawa Y, Ishii A, Wakunami K, Ichihashi Y, Oi R. Two-step phase-shifting interferometry for self-interference digital holography. Optics Letters. 2021;**46**:669-672. DOI: 10.1364/OL.414083

[49] Rosen J, Alford S, Anand V, Art J, Bouchal P, Bouchal Z, et al. Roadmap on recent progress in FINCH technology. Journal of Imaging. 2021;**7**:197. DOI: 10.3390/jimaging7100197

[50] Zhou H, Huang L, Li X, Li X, Geng G, An K, et al. All-dielectric bifocal isotropic metalens for a single-shot hologram generation device. Optics Express. 2020;**28**:21549-21559. DOI: 10.1364/OE.396372

[51] Choi K, Yim J, Yoo S, Min SW. Self-interference digital holography with a geometric-phase hologram lens. Optics Letters. 2017;**42**:3940-3943. DOI: 10.1364/OL.42.003940

[52] Vijayakumar A, Bhattacharya S. Characterization and correction of spherical aberration due to glass substrate in the design and fabrication of Fresnel zone lenses. Applied Optics. 2013;**52**:5932-5940. DOI: 10.1364/AO.52.005932

[53] Tahara T, Oi R. Palm-sized single-shot phase-shifting incoherent digital holography system. OSA Continuum. 2021;**4**:2372-2380. DOI: 10.1364/OSAC.431930

[54] Anand V, Rosen J, Juodkazis S. Review of engineering techniques in chaotic coded aperture imagers. Light: Advanced Manufacturing. 2022;**3**:1-3. DOI: 10.37188/lam.2022.024

[55] Zalevsky Z, Mendlovic D, Dorsch RG. Gerchberg–Saxton algorithm applied in the fractional Fourier or the Fresnel domain. Optics Letters. 1996;**21**: 842-844. DOI: 10.1364/OL.21.000842

[56] Rai MR, Rosen J. Noise suppression by controlling the sparsity of the point spread function in interferenceless coded aperture correlation holography (I-COACH). Optics Express. 2019;**27**: 24311-24323

[57] Liu C, Man T, Wan Y. High-quality interferenceless coded aperture correlation holography with optimized high SNR holograms. Applied Optics. 2022;**61**(3):661-668. DOI: 10.1364/AO.444783

[58] Anand V, Ng SH, Maksimovic J, Linklater D, Katkus T, Ivanova EP, et al. Single shot multispectral multidimensional imaging using chaotic waves. Scientific Reports. 2020;**10**:1-3. DOI: 10.1038/s41598-020-70849-7

[59] Anand V, Ng SH, Katkus T, Juodkazis S. Spatio-spectral-temporal imaging of fast transient phenomena using a random array of pinholes. Advanced Photonics Research. 2021;**2**: 2000032. DOI: 10.1002/adpr.202000032

[60] Anand V, Ng SH, Katkus T, Juodkazis S. White light three-dimensional imaging using a quasi-random lens. Optics Express. 2021;**29**: 15551-15563. DOI: 10.1364/OE.426021

[61] Kumar M, Vijayakumar A, Rosen J. Incoherent digital holograms acquired by interferenceless coded aperture correlation holography system without

refractive lenses. Scientific Reports. 2017;**7**:1-11. DOI: 10.1038/s41598-017-11731-x

[62] Antipa N, Kuo G, Heckel R, Mildenhall B, Bostan E, Ng R, et al. DiffuserCam: Lensless single-exposure 3D imaging. Optica. 2018;**5**:1-9. DOI: 10.1364/OPTICA.5.000001

[63] Sahoo SK, Tang D, Dang C. Single-shot multispectral imaging with a monochromatic camera. Optica. 2017;**4**: 1209-1213. DOI: 10.1364/OPTICA.4.001209

[64] Lee K, Park Y. Exploiting the speckle-correlation scattering matrix for a compact reference-free holographic image sensor. Nature Communications. 2016;**7**:1-7. DOI: 10.1038/ncomms13359

[65] Sun YK, Wang L, Kamano M, Juodkazis S. Plasmonic nano-imprinting by photo-doping. Optics Letters. 2018; **43**:3786-3789. DOI: 10.1364/OL.43.003786

[66] Lu YM, Liu XQ, Zhu L, Chen QD, Juodkazis S, Sun HB. Vector scanning subtractive manufacturing technology for laser rapid fabrication. Optics Letters. 2021;**46**:1963-1966. DOI: 10.1364/OL.422455

[67] Hua JG, Tian ZN, Xu SJ, Lundgaard S, Juodkazis S. Fast fabrication of optical vortex generators by femtosecond laser ablation. Applied Surface Science. 2019;**475**:660-665. DOI: 10.1016/j.apsusc.2018.12.249

[68] Linklater DP, Juodkazis S, Ivanova EP. Nanofabrication of mechano-bactericidal surfaces. Nanoscale. 2017;**9**:16564-16585. DOI: 10.1039/C7NR05881K

[69] Nieminen TA, Knöner G, Heckenberg NR, Rubinsztein-Dunlop H. Physics of optical tweezers. Methods in Cell Biology. 2007;**82**:207-236. DOI: 10.1016/S0091-679X(06)82006-6

[70] Polimeno P, Magazzu A, Iati MA, Patti F, Saija R, Boschi CD, et al. Optical tweezers and their applications. Journal of Quantitative Spectroscopy and Radiative Transfer. 2018;**218**:131-150. DOI: 10.1016/j.jqsrt.2018.07.013

[71] Ashkin A. Acceleration and trapping of particles by radiation pressure. Physical Review Letters. 1970;**24**:156. DOI: 10.1103/PhysRevLett.24.156

[72] Molloy JE, Padgett MJ. Lights, action: Optical tweezers. Contemporary Physics. 2002;**43**:241-258. DOI: 10.1080/00107510110116051

[73] Curtis JE, Koss BA, Grier DG. Dynamic holographic optical tweezers. Optics Communication. 2002;**207**: 169-175. DOI: 10.1016/S0030-4018(02)01524-9

[74] Balasubramani V, Kuś A, Tu HY, Cheng CJ, Baczewska M, Krauze W, et al. Holographic tomography: Techniques and biomedical applications. Applied Optics. 2021;**60**:B65-B80. DOI: 10.1364/AO.416902

[75] Vijayakumar A, Vinoth B, Minin IV, Rosen J, Minin OV, Cheng CJ. Experimental demonstration of square Fresnel zone plate with chiral side lobes. Applied Optics. 2017;**56**:F128-F133. DOI: 10.1364/AO.56.00F128

[76] Balasubramani V, Tu HY, Lai XJ, Cheng CJ. Adaptive wavefront correction structured illumination holographic tomography. Scientific Reports. 2019;**9**(1):1-7. DOI: 10.1038/s41598-019-46951-w

[77] Smith D, Ng SH, Han M, Katkus T, Anand V, Glazebrook K, et al. Imaging

with diffractive axicons rapidly milled on sapphire by femtosecond laser ablation. Applied Physics B. 2021;**127**: 1-11. DOI: 10.1007/s00340-021-07701-x

[78] Mao T, Ma X, Cuadros AP, Dai X, Wang Z, Zhang X, et al. Static coded aperture in robotic X-ray tomography systems. Optics Express. 2022;**30**: 7677-7693. DOI: 10.1364/OE.449505

[79] Smith D, Gopinath S, Arockiaraj FG, Reddy ANK, Balasubramani V, Kumar R, et al. Nonlinear reconstruction of images from patterns generated by deterministic or random optical masks–concepts and review of research. Journal of Imaging. 2022;**8**(6):174. DOI: 10.3390/jimaging8060174